High-Speed Infrared Thermography for Measuring Flash Temperatures in Sheared Fault Gouge Analogues

Chien-Cheng Hung[1, 2, 3] and André R. Niemeijer[1]

[1] *Department of Earth Sciences, Utrecht University, Utrecht, The Netherlands*

[2] *Department of Earth Sciences, National Central University, Taoyuan, Taiwan*

[3] *Institute of Earth Sciences, Academia Sinica, Taipei, Taiwan*

Corresponding author: Chien-Cheng Hung (e-mail: c.hung@uu.nl)

Abstract

Flash temperatures induced by flash heating can lead to thermal softening or decomposition of fault-zone materials at microscopic grain contacts and, consequently, cause a rapid reduction in fault strength during seismic slip. To quantify the efficiency of short-term frictional heating at the contact scales and its impact on the mechanical fault strength, we conducted rotary-shear friction experiments on Ottawa quartz sand "gouges" with variable grain sizes of 250–710 μm at a range of normal stresses of 1–7.5 MPa and slip velocities of 1–50 mm/s under room-dry and wet conditions. We employed a high-speed infrared camera to monitor temperature fluctuations along the outer circumference of the ring-shaped gouge layer during sliding, utilizing a frame rate of up to 1200 Hz with a spatial resolution of 15 μm to capture flash temperature occurring at asperity contacts. We show that flash temperature can be captured within the gouge layer in both room-dry and wet conditions with a peak value up to ~220°C and ~100°C, respectively. In addition, the flash temperature increases with increasing slip velocity and grain size, while decreasing at higher normal stress, which is likely associated with enhanced grain size reduction. In our study, we showed that flash

temperatures in shearing fault gouges can be constrained using a fast thermal camera. Although difficulties remain in the experimental set-up related to the need to confine the gouge layer and to the evolution of contact size due grain size reductions, the trends in maximum temperatures we observed agree with those predicted from theory.

1. Introduction

Characterizing temperature rise from frictional sliding is crucial to understanding the thermally activated mechanisms that cause faults to weaken during coseismic slip and associated earthquake rupture propagation (Rice, 2006). Several theoretical and experimental studies have proposed various dynamic weakening mechanisms, depending on fault rock composition and experimental conditions, to account for the reduction in friction coefficient seen when sliding velocities approach seismic slip rates ($V > 0.01$ m/s; see Di Toro et al., 2010, Niemeijer et al., 2012, and Tullis, 2015 for summaries). Among these weakening mechanisms, flash heating at highly stressed asperity contacts is believed to be one of the main mechanisms causing dramatic weakening at the onset of rock-on-rock slip (e.g. Goldsby and Tullis, 2011; Kohli et al., 2011; Spagnuolo et al., 2015) and shearing of gouge materials (e.g. Yao et al., 2016a, b). So far, the inferred role of flash heating and weakening is generally based on predictions using a flash-heating model (Beeler et al., 2008; Brantut and Platt, 2017; Proctor et al., 2014; Rice, 2006; Yao et al., 2018) and/or the microstructural evidence of thermal softening (e.g. local melting) at asperity contact scales (e.g. Acosta et al., 2018). Recent studies using laboratory friction experiments by Saber (2017) and Barbery et al. (2021, 2023) have shown that surface temperature increases at contact points on sliding surfaces between Westerly granite blocks, under room-dry conditions, can be successfully captured by employing a high-speed infrared camera (a frame rate

51   of 300 Hz and a resolution of 75 μm). These authors documented that flash temperatures

52   and stress distribution are highly heterogeneous at the rock-on-rock interface during

53   seismic slip. In addition, no evidence of dynamic weakening was detected, as the

54   measured surface temperatures did not approach the weakening temperature inferred

55   for granite (~800°C). This may also reflect wear processes that reduce local normal

56   stresses and increase the true contact area during slip, thereby suppressing conditions

57   favorable for flash heating. Currently, experimental constraints on flash temperatures

58   in a sheared granular gouge layer are lacking. In particular, direct detection of thermal

59   signals, from flash heating occurring within a shearing gouge layer, remains

60   challenging due to difficulties with gouge confinement, the small scale of grain contact

61   asperities (<<1 mm), and short contact lifetimes (ms).

62

63   In an attempt to make new progress, we developed an experimental setup, with a

64   high-speed infrared camera, that allows us to acquire in-situ thermal images across the

65   entire thickness of the gouge layer during rapid shearing under room-dry and wet

66   conditions. In this study, we aim to experimentally characterize the dependence of peak

67   flash temperature on normal stress, slip velocity, and grain size to better understand

68   how flash heating is influenced by these variables, and to assess whether the results are

69   consistent with the predictions of previous theoretical analyses (Rice, 2006; Proctor et

70   al., 2014; Brantut and Platt, 2017).

71

72   **2. Materials and Methods**

73   **2.1 Starting materials**

74   We used ASTM standard C778 Ottawa quartz sand obtained from the U.S. Silica

75   Company (Ottawa, IL, USA) as starting materials. The materials contain a SiO_2 content

76 of 99.7 wt%, minor quantities of Al_2O_3 (0.06 wt%), Fe_2O_3 (0.02 wt%), and TiO_2 (0.01

77 wt%). Scanning electron microscopy showed that most sand grains are well-rounded,

78 with smooth surfaces characterized by pressure solution indentations and quartz

79 overgrowths (Hangx and Brantut, 2019). We prepared four fractions of the sand with

80 grain sizes of 250–300 μm, 300–425 μm, 425–500 μm, and 500–710 μm by double-

81 sieving the material as received. We adopted the grain size fraction 425–500 μm as the

82 reference grain size for most of the experiments. For each experiment, we used 35

83 grams of the Ottawa sand gouge, which results in an initial gouge thickness of ~4.5 mm

84 after normal loading at 2.5 MPa (effective) normal stress and before shearing.

85

86 **2.2 Rotary-Shear Friction Experiments**

87 We performed medium-velocity friction experiments using a rotary-shear

88 apparatus (RAP; Korkolis, 2019) plus a high-speed infrared camera (Figure 1a). The

89 RAP consists of a torque reaction frame that is housed inside an Instron 8862 testing

90 machine equipped with a servo-controlled electromechanical actuator that may be

91 operated either in position control (±50 mm range, 5 μm resolution) or in load control

92 mode (±100 kN range, 0.008 kN resolution). Within the RAP, we developed a gouge

93 setup that allows us to confine gouge samples and pressurize the pore fluid within the

94 simulated fault zone during rapid sliding (Figure 1b). The gouge layer is confined

95 between two ring-shaped, steel pistons (100-mm external, 70-mm internal diameters),

96 allowing loading in the axial direction. The piston faces are toothed, with the teeth

97 spaced at 1.5 degree (240 teeth on the full ring) and their height varies from the inside

98 diameter of 0.62 mm to the outside diameter of 0.96 mm. In the middle, the height is

99 0.79 mm. All teeth are oriented perpendicular to the direction of sliding. A brass outer

100 and inner rings were used to confine the gouge layer laterally to avoid gouge extrusion

101   during shearing. The driving platen is equipped with two angular potentiometers (0.001

102   degrees, or about 0.74 μm resolution) that measure its rotation. A pair of load cells (20

103   kN range, 0.008 kN resolution), mounted on opposite sides of a horizontal steel block

104   ("crosshead"; Figure 1a), measure the reaction force of the frame due to the rotation

105   imposed by the motor. Axial displacment is tracked by measuring the change in the load

106   frame position under load control. Local pore fluid pressure changes during sliding

107   were measured using two pressure transducers (10 MPa full range, with 0.01 MPa

108   resolution and less than 10 ms response time) installed at opposite sides, and at identical

109   radial position (centered at $d = 85$ mm), in the bottom rotary piston (Figure 1b). To

110   detect thermal signals across the full gouge layer thickness, we installed a circular,

111   transparent sapphire window (10 mm in diameter and 2 mm in thickness) in the outer

112   confining ring (Figure 1c, d). The screw-in design of the window allows its position to

113   be adjusted to be as close as possible to (in contact with) the gouge layer.

114
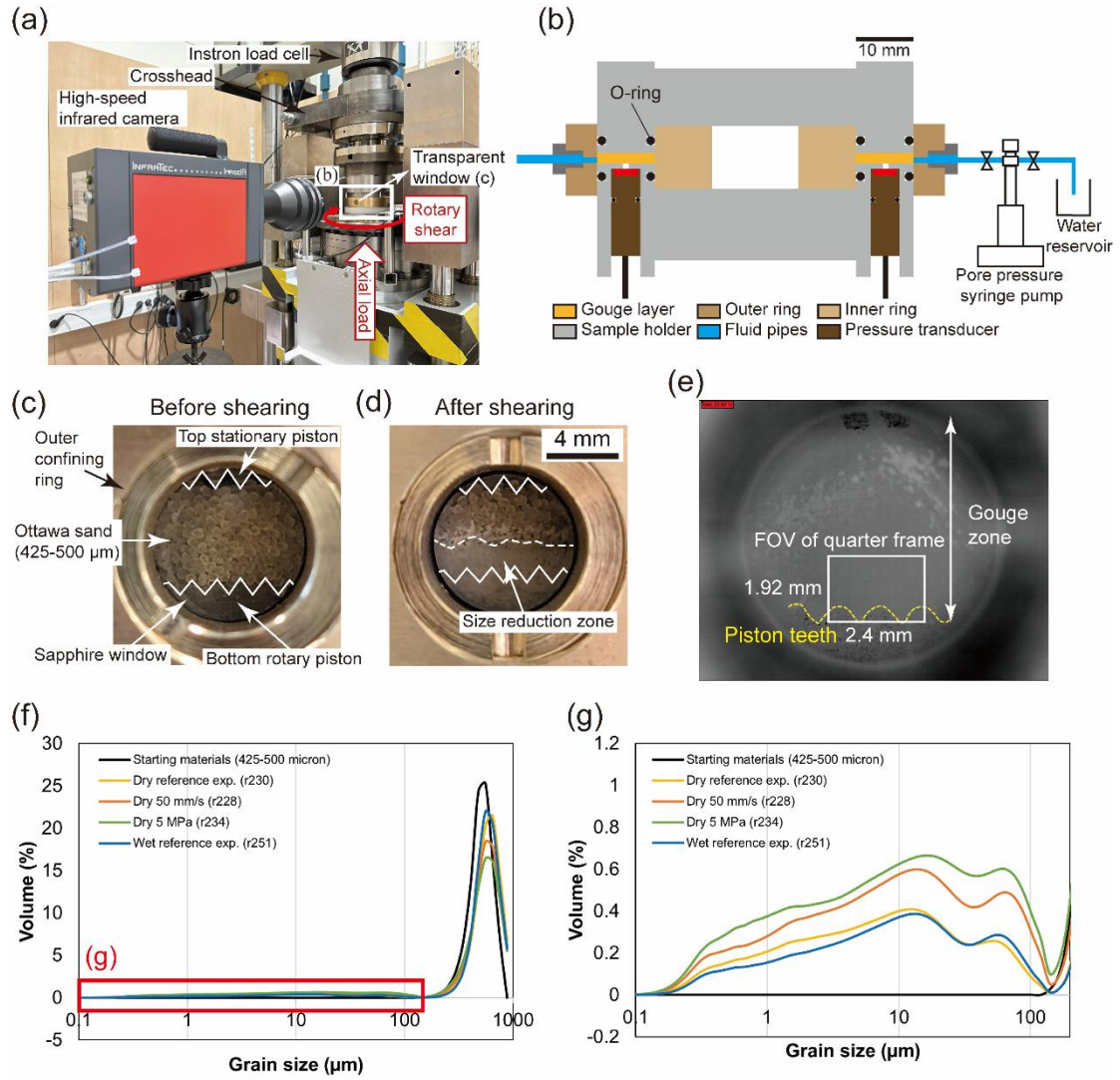
Figure 1. Experimental setup. (a) Photograph of the pressurized gouge setup installed in the rotary-shear apparatus (RAP) with the high-speed infrared camera. (b) Cross-section of the pressurized gouge setup. Pressure transducers are installed in the bottom rotary piston at ~2 mm distance from the gouge layer. The pore fluid inlet and outlet are at 135 and 45 degrees to the sapphire window, respectively. (c) Photograph of the profile of the undeformed, room-dry Ottawa sand gouge layer, sandwiched between the pistons, and laterally confined by an outer brass ring with a transparent sapphire window. (d) Photograph of a deformed room-dry gouge layer showing a zone/layer of reduced grains. (e) Thermography of the gouge layer before sliding under a full-frame field of view (FOV) (9.6 mm × 7.68 mm). The white rectangle indicates the field of

view (FOV: 2.4 mm × 1.92 mm) under quarter-frame analyses (1200 Hz) applied in all our tests. (f) Particle size distribution (PSD) of the starting materials (425-500 μm Ottawa sand gouge) and the deformed samples with the same initial grain size under different conditions, plotted as volume percentage vs. grain size. Reference experiment refers to a normal stress of 2.5 MPa and slip velocity of 10 mm/s (g) Zoom-in PSD for grain sizes 0.1–100 μm.

Friction experiments were conducted on both room-dry and wet gouges at an applied normal stress σ_n of 1.0–7.5 MPa and a constant slip velocity V in the range 1–50 mm/s, reaching a total displacement of up to 750 mm (equivalent to ~2.8 of full rotations of the piston assembly). Grain comminution was lowest in our experiments at lower normal stresses and sliding velocities, as shown in the particle size distribution anaylsis (Figure 1f, g). Thus, we chose a normal stress of 2.5 MPa and a slip velocity of 10 mm/s as the reference conditions at which flash heating could be resolved spatially. Before applying the normal load to the target value, wet gouges were prepared by saturating the sample with DI water using a syringe pump (ISCO pump; Figure 1b) through the pore fluid inlet port until water came out of the outlet drainage ports, without bubbles. All wet experiments were conducted under undrained conditions at initially atmospheric pore pressure conditions (i.e. 0.1 MPa) by keeping the outlet ports closed during shearing. After the target normal stress was applied, we initiated shearing of the gouge sample, recording the thermal imaging at synchronized time. During the entire experiment, data on shear stress τ, normal stress σ_n, axial displacement, and velocity V, were obtained at a logging rate of 5 kHz. All the tests performed are listed in Table 1.

151 ***Table 1.*** *List of experiments and conditions with the average temperature increase ΔT_{avg}*

152 *as well as the measured and predicted (see equation 1) flash temperatures T_{max}. The IR*

153 *temperature range chosen for the room-dry and wet experiments is 60–200°C and 30–*

154 *150°C, respectively. We define a flash as a maximum temperature measurement in a*

155 *single frame that is larger (>50°C for dry, >4°C for wet) than the maximum*

156 *temperatures in neighbouring frames. Predictions of flash temperature for wet*

157 *conditions are not included.*

ID	σ_n (MPa)	Pore fluid	V (mm/s)	D (mm)	Grain size (mm)	Number of flashes	ΔT_{avg} (°C)	Measured T_{max} (°C)	Predicted T_{max} (°C)
					Room-dry conditions				
r228	2.5	-	50	500	0.425-0.5	30	61.84	183.54	568.95
r229	2.5	-	25	750	0.425-0.5	31	55.87	222.60	408.17
r230*	2.5	-	10	750	0.425-0.5	23	48.42	137.72	265.50
r231	2.5	-	1	75	0.425-0.5	N/A	12.42	N/A	97.63
r232	2.5	-	5	600	0.425-0.5	23	38.82	124.25	193.59
r234	5	-	10	750	0.425-0.5	28	50.92	N/A	291.41
r235	1	-	10	400	0.425-0.5	27	36.44	123.96	228.63
r236	7.5	-	10	200	0.425-0.5	1	52.37	90.26	309.32
r237	2	-	10	750	0.425-0.5	15	49.68	221.98	251.46
r238	3	-	10	750	0.425-0.5	22	45	169.36	272.23
r239	7.5	-	50	450	0.425-0.5	1	73.24	101.34	666.94
r240	2.5	-	10	750	0.3-0.425	23	53.62	125.88	228.63
r241	2.5	-	10	750	0.25-0.3	2	52.69	119.03	202.98
r242	2.5	-	50	750	0.25-0.3	4	60.83	150.07	429.16
r245	2.5	-	10	750	0.5-0.71	30	53.33	222.60	297.51
					Wet conditions				
r249	2.5	DI water	50	750	0.425-0.5	3	8.74	81.74	-
r251*	2.5	DI water	10	750	0.425-0.5	13	5.28	43.74	-
r254	5	DI water	10	750	0.425-0.5	27	4.69	158.40	-
r255	5	DI water	50	750	0.425-0.5	43	7.32	61.67	-
r256	7.5	DI water	10	750	0.425-0.5	15	5.22	85.42	-
r257	4	DI water	10	750	0.425-0.5	6	3.77	44.17	-
r258	6	DI water	10	750	0.425-0.5	4	3.18	38.40	-
r259	2.5	DI water	10	750	0.5-0.71	5	3.85	40.09	-
r260	2.5	DI water	10	750	0.25-0.3	*N/A*	3.49	*N/A*	-

2.3 High-Speed Infrared Thermal Imaging of Gouge Profiles

We used an Infratec ImageIR 8300hp infrared camera with a precision microscope lens M=1.0x and a working distance of 20 cm (Figure 1a) to provide the requirements for high-speed thermography. The combined setup has a detector format of 640 × 512 pixels and a wide range of IR frame capture rates from up to 355 Hz (a full frame window size) to up to 5000 Hz (a line measurement) with a spatial resolution down to 15 μm per pixel. All the infrared radiation (IR) signals acquired from the infrared camera were processed using IRBIS® 3.1 Infrared Thermographic Software (https://www.infratec.eu/thermography/thermographic-software/) to convert the digital IR signal data to thermographs (i.e. temperature distributions) with the user choice calibration (e.g. emission, absorption, and transmission). In this study, we took an emissivity of 1 (full reflection of IR from the object), an absorption coefficient of 0 (no attenuation of IR), and a transmission of 1 (full penetration of incident IR) as the inputs for the calibration of the IR signal to arrive at the target object temperature in the software. We have not taken the effects of mineralogy, the sapphire window or the presence of water on the IR signal into account in the present work. The focus of the lens was adjusted until the piston teeth were visible in the gouge layer on the real-time thermograph (Figure 1e). During shearing of each experiment, we adopted a quarter-frame analysis of up to 1200 Hz (~0.83 ms) with a field of view (FOV) of 2.4 mm × 1.92 mm and a spatial resolution of 15 μm per pixel to capture thermographs that emerged from the FOV of the gouge shear zone. These mostly covered the bottom third

183 of the gouge layer (i.e. rotating side) plus a small portion of the piston teeth (Figure 1c,

184 e). For experiments conducted at the chosen reference conditions (ID r230, r251), a

185 sequence of at least 90000 thermographs (75 seconds × 1200 Hz) was acquired from

186 the FOV throughout the experiment. The IR camera is equipped with a neutral density

187 filter and is capable of measurements over several pre-set, calibrated temperature

188 ranges with multiple integration times. We took the factory-calibrated settings for two

189 different IR temperature ranges of 60–200°C and 30–150°C, for room-dry and wet test

190 conditions, respectively. After each experiment, we exported the maximum

191 temperatures and the corresponding location (X and Y coordinates), as well as the

192 average temperatures over the FOV of every acquired thermograph, to investigate the

193 temporal and spatial evolution of peak temperatures with displacement.

194

195 **3. Results**

196 **3.1 Mechanical Behavior**

197 Figure 2 shows the evolution of apparent friction μ_{app} (= shear stress τ / applied

198 normal stress σ_n) against displacement obtained for the room-dry and wet gouges at the

199 variable slip velocities, normal stresses, and initial grain sizes shown. For the room-dry

200 gouges (Figure 2a, c, e), the frictional evolution is generally similar, regardless of slip

201 velocity, normal stress, and grain size. Specifically, μ_{app} firstly overcomes a "static"

202 peak friction μ_s of ~0.9, soon after slip initiation, subsequently rapidly drops to a

203 constant (dynamic) level of ~0.65 within ~0.3 m displacement. This is followed by

204 minor displacement weakening beyond the first full rotation (~267 mm displacement)

205 reaching a near-constant value of ~ 0.6 during the late stage of slip. The overall level

206 of friction systematically decreases with increasing normal stress (Figure 2c), with the

207 exception of the experiment conducted at 5 MPa normal stress (ID r234), which shows

208 anomalous behavior in the form of marked displacement strengthening after one

209 rotation. This is likely due to jamming of material between the piston and the confining

210 ring.

211

212   For the wet gouges (Figure 2b, d, f, and 3), the initial frictional behavior is similar

213 to the room-dry gouges, featuring a peak μ_{app} value μ_s of ~0.9 followed by a sharp

214 friction drop. Different levels of slip weakening occur depending on the slip velocity,

215 normal stress, and grain size. At a normal stress of 2.5 MPa, the wet gouge subjected to

216 a slip velocity of 50 mm/s showed increased slip-weakening towards a lower dynamic

217 friction of ~0.45, compared with the behavior seen at the lower slip velocity of 10 mm/s

218 (Figure 2b) or in dry samples. At a slip velocity of 10 mm/s, the wet gouges significantly

219 slip-weaken only when the normal stress is equal to or greater than 4 MPa. Under these

220 conditions, the onset of weakening starts earlier and the dynamic friction level

221 decreases with increasing normal stress (Figure 2d). Increased slip weakening is also

222 observed, compared with the reference test, when the grain size is either greater or

223 smaller than the reference value, without any systematic correlation between grain size

224 and the level of dynamic friction (Figure 2f).

225
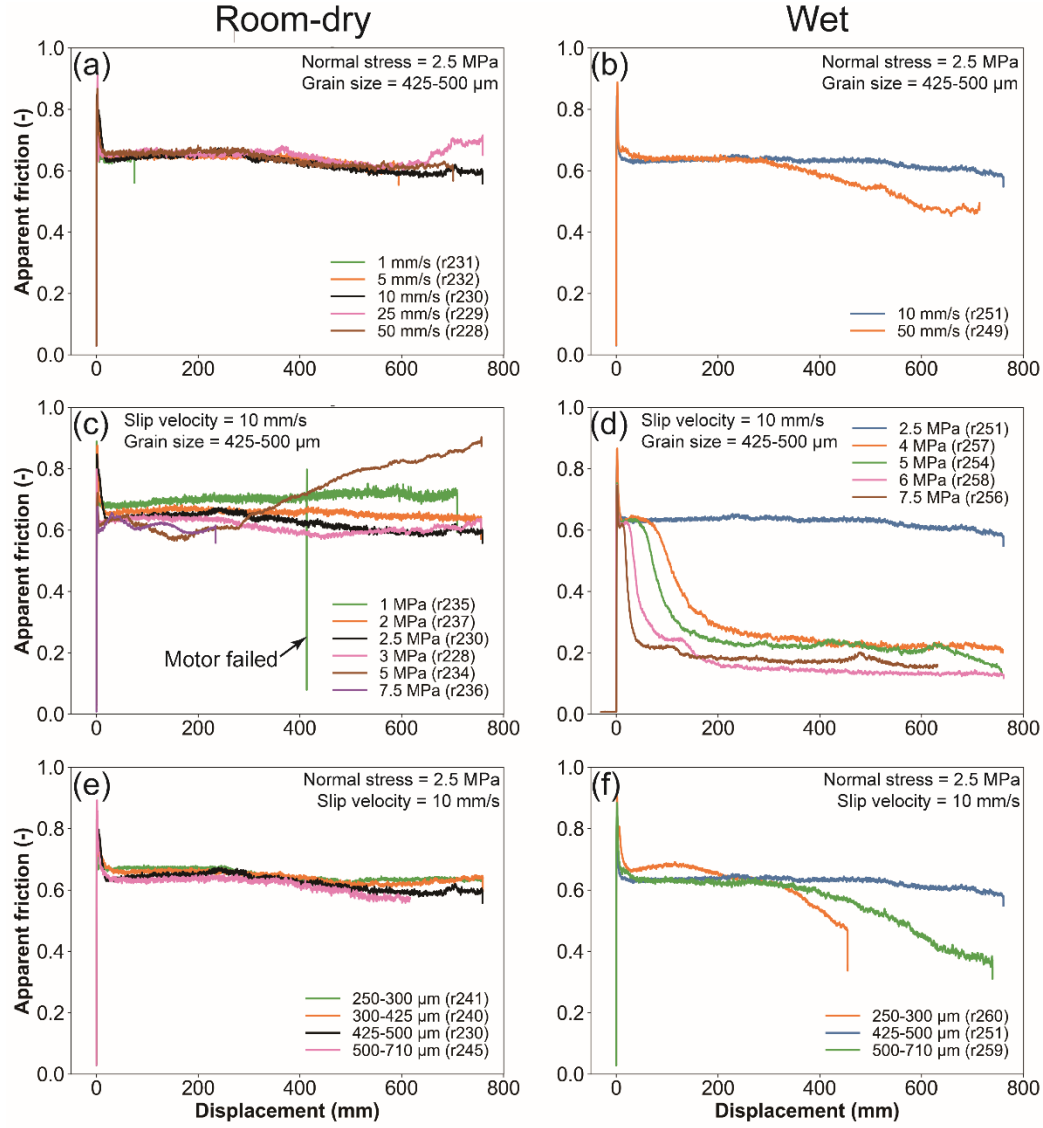
Figure 2. Evolution of apparent friction μ_{app} as a function of displacement for room-dry (a, c, e) and wet gouges (b, d, f) under variable slip velocities, normal stresses, and initial grain sizes. The sudden friction drop observed in (c), the green curve, is the result of re-shear due to a motor failure.

Fluid pressure increases were always observed in the wet experiments at the displacement at which weakening starts (i.e. beyond the peak static friction; see Figure 3). This shows that the fluid pressure increase has a positive correlation with applied normal stress, since the maximum fluid pressure increased from ~3.5 MPa, at a normal

236 stress of 4 MPa, to ~7 MPa at a normal stress of 7.5 MPa. In addition, each experiment

237 shows a sudden gouge dilatation during the attainment of peak friction, followed by

238 ongoing gouge compaction (Figure 3). The amount of compaction shows the same trend

239 with normal stress as fluid pressure, i.e. more compaction occurs in experiments with

240 higher normal stress.

241

242
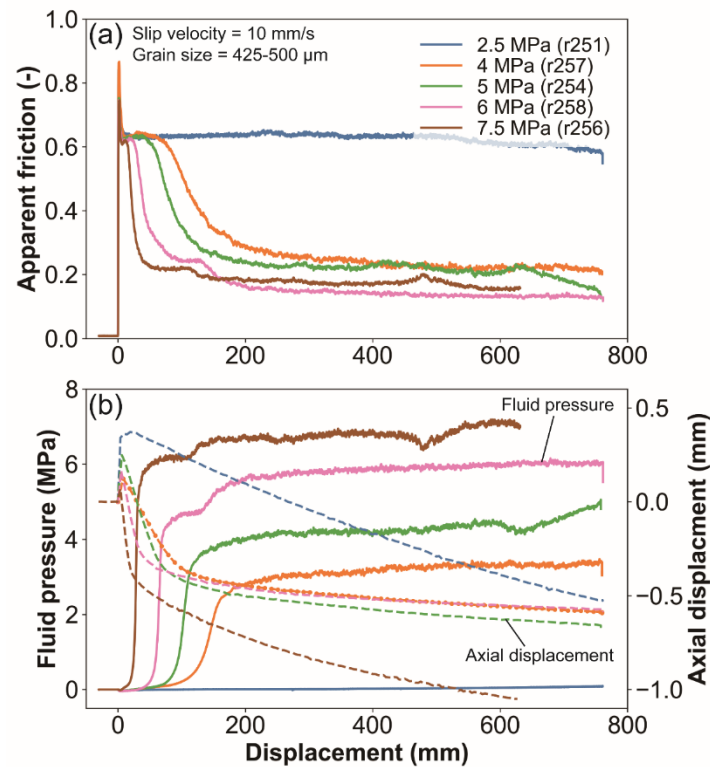
243 **Figure 3.** Evolution of (a) apparent friction and (b) pore fluid pressure and axial

244 displacement, as a function of shear displacement for the wet experiments at a slip

245 velocity of 10 mm/s, using an initial grain size of 425–500 μm. Dashed curves in (b)

246 represent axial displacement data whereby positive values indicate dilatation and

247 negative values indicate compaction. Solid curves in (b) represent pore fluid pressure

248 in these undrained tests.

249

250 **3.2 Evolution of Maximum Temperature Rise with Displacement**

251   The maximum temperatures obtained from each thermal image are plotted as a

252   function of displacement in Figures 4, 5, and 6. Generally, multiple temperature peaks

253   (i.e. spikes) with a duration of one frame (~0.83 ms) can be observed, representing

254   flashes in most experiments with the largest peak temperatures being ~220°C and

255   ~100°C in the room-dry and wet gouges, respectively. For most of the experiments, the

256   maximum temperatures in the FOV showed a rapid increase after the slip initiation,

257   with a faster rise with increasing velocity, but then soon reached a plateau (at a base

258   level of ~25–40°C), which becomes higher at higher velocity (Figure 4). The presence

259   of a temperature plateau is due to the settings of the IR temperature measurement range

260   (60–200°C and 30–150°C for room-dry and wet experiments, respectively); below the

261   lower bound of the range, temperature cannot be accurately determined or displayed.

262   Another thing that should be noted is that Figures 4, 5, and 6 include all thermal flashes

263   that occurred within the full FOV throughout the entire slip period of each experiment.

264   Thus, the observed flashes might not only result from the sliding between grain-grain

265   contacts but also from sliding between the grains and the window as well as between

266   the grains and the piston, due to gouge extrusion or grain fragments jamming between

267   the sapphire window and the piston.

268

269   Nonetheless, these results still provide insight into systematic differences in the

270   evolution of temperature and the magnitude of the peak temperatures. Overall, we

271   observed that peak temperature rises are significantly reduced in the presence of water,

272   and the peak temperature systematically increases with increasing slip velocity (Figure

273   4). In both the room-dry and wet gouges, the number of flashes becomes much less and

274   their magnitudes become much lower at the lowest applied slip velocity of 1 mm/s. In

275 the dry experiments, the magnitude of the flashes appears to be the greatest (up to 200°C)

276 at 2.5 MPa, while becoming less significant with both decreasing and increasing normal

277 stress (Figure 5a). The dependence of peak temperature on normal stress is not visible

278 in the wet experiments (Figure 5b). Note that the dry experiment (ID r236) at 7.5 MPa

279 normal stress was terminated soon (~3 seconds) after slip initiation (Figure 5a) because

280 of sounds indicating unwanted abrasion of the outer ring. For the range of grain sizes

281 explored, the variations in the magnitudes of flashes are similar in both the dry and wet

282 tests and are difficult to quantify based on these data (Figure 6).

283
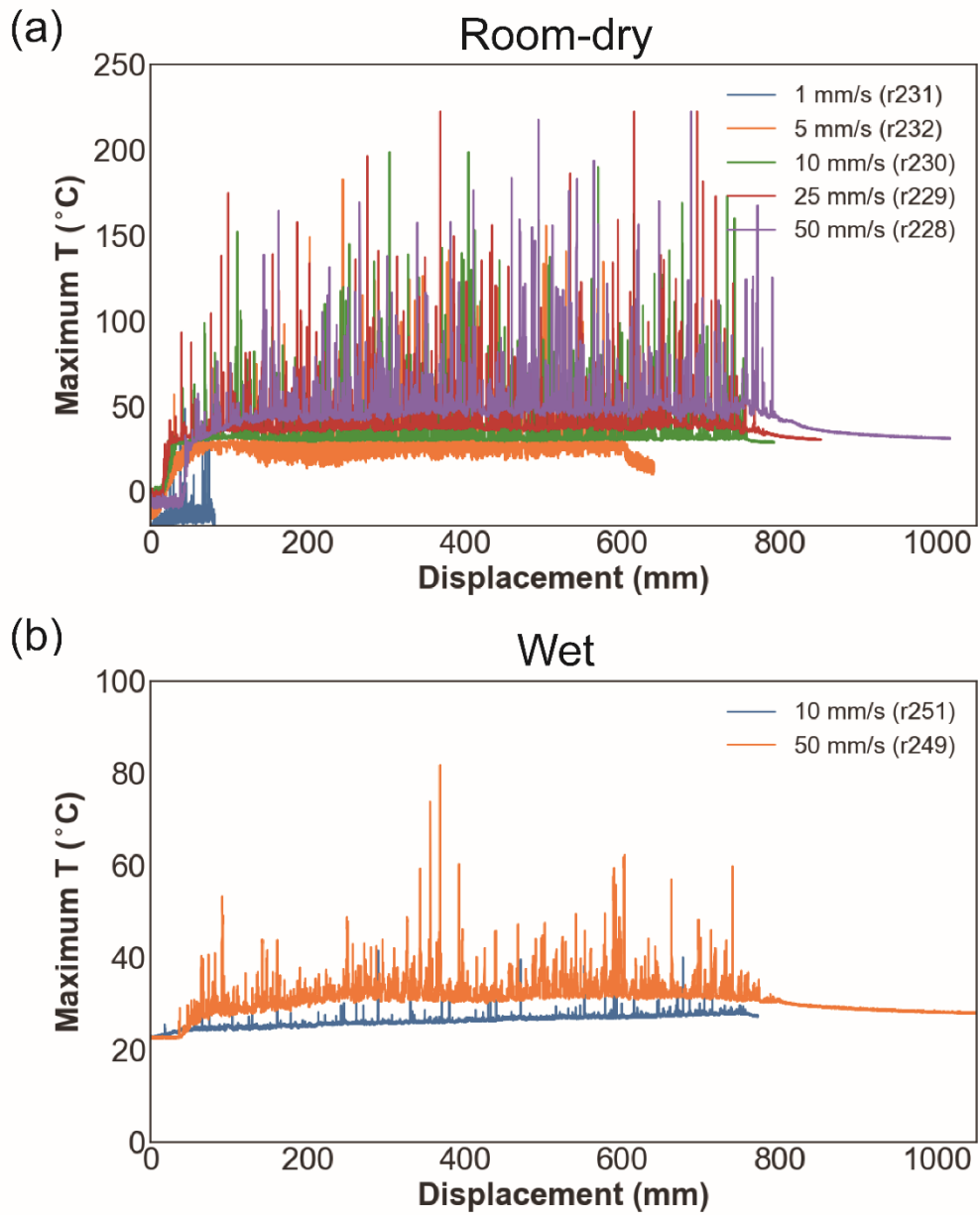
Figure 4. Evolution of maximum temperature within the FOV (4 mm × 3.2 mm) as a

function of displacement for the room-dry gouges (a) and the wet gouges (b) tested at

a normal stress of 2.5 MPa and different slip velocities.

287

288
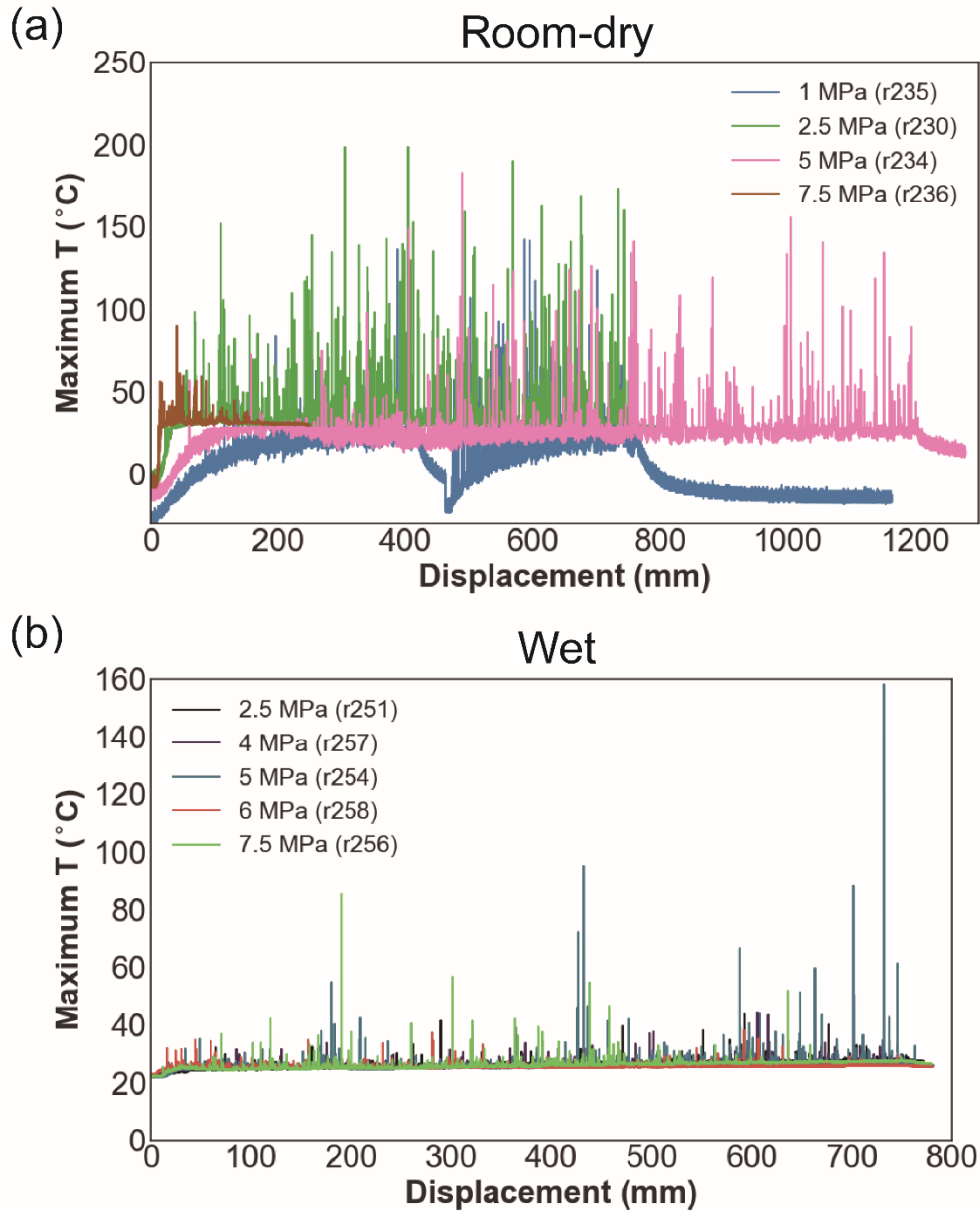
Figure 5. Evolution of maximum temperature within the FOV (4 mm × 3.2 mm) as a function of displacement for the room-dry gouges (a) and the wet gouges (b) tested at a slip velocity of 10 mm/s and different normal stresses. The temporary decrease in the minimum measured temperature at normal stress of 1 MPa results from an unintended stop in shearing at ~40 seconds due to a motor break.

294
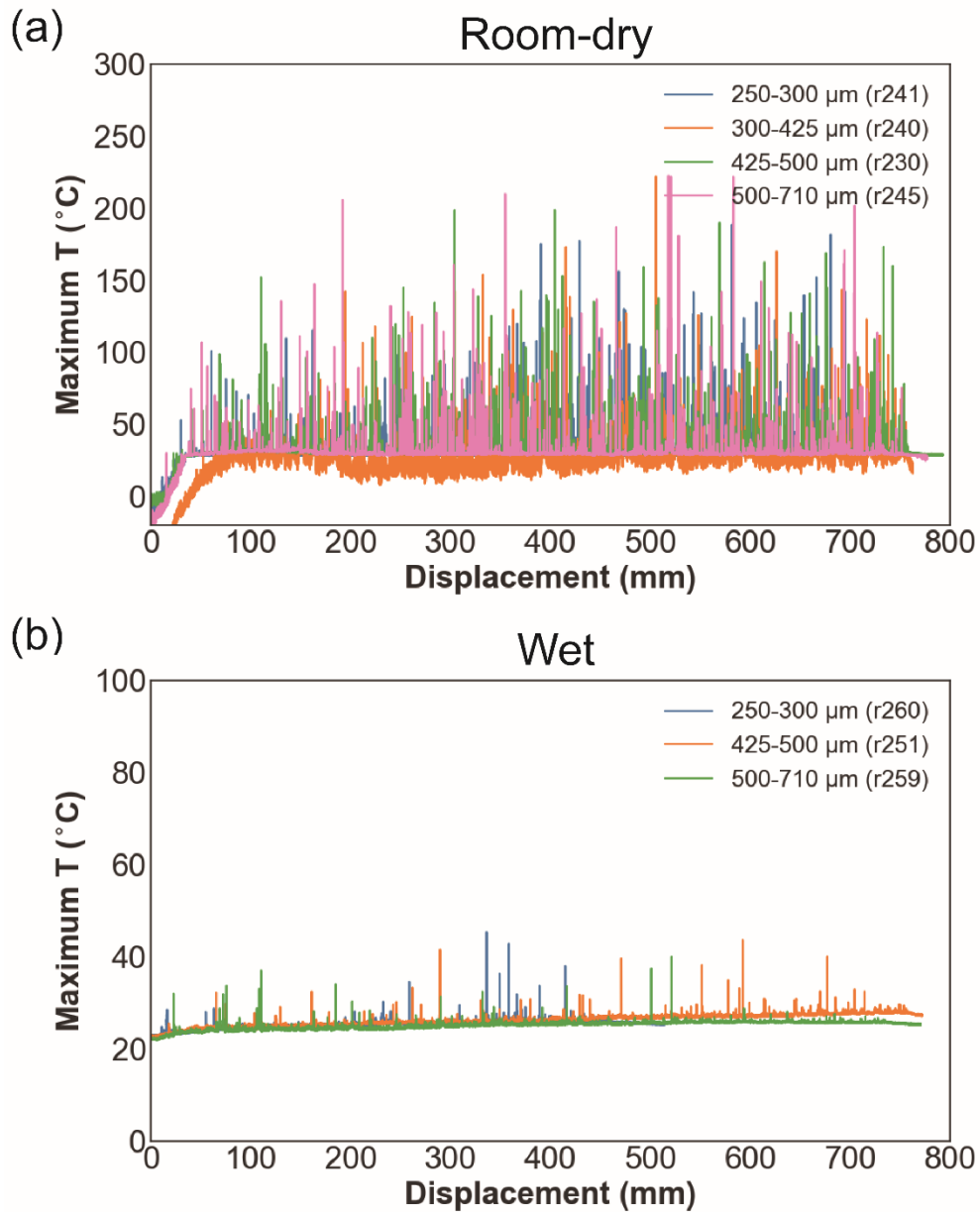
Figure 6. Evolution of maximum temperature within the FOV (4 mm × 3.2 mm) as a function of displacement for the room-dry gouges (a) and the wet gouges (b) tested at a normal stress of 2.5 MPa and a slip velocity of 10 mm/s, with different initial grain sizes.

3.3 Spatial and Temporal Distributions of Flashes

We located the position of the thermal flashes to see if they occurred within the actual gouge zone, as opposed to the portion of the FOV below the teeth tops. Figure 7

304   presents the spatial and temporal distributions of the flashes, here taken as those frames

305   (duration ~0.83 ms) with temperature rise ΔT larger than 50°C and 4°C, for the

306   reference room-dry and wet gouges, respectively. These results exclude the flashes with

307   a position at and below the horizontal level (i.e. Y position) of the teeth tops on the

308   bottom rotary piston (dashed lines). This is to rule out the flashes that potentially

309   resulted from sliding between the grains and the piston / window. After filtering out

310   data from below the chosen moving datum, we still observed many flashes, which we

311   infer occurred within the main gouge zone. The peak temperature and the number of

312   these flashes in each experiment are summarized in Table 1. Generally, in terms of

313   spatial distribution, flashes tend to be concentrated within a narrow zone (~500 μm

314   thick) under room-dry conditions (Figure 7a, b) whereas flashes are more separated

315   under wet conditions.

316

317

318
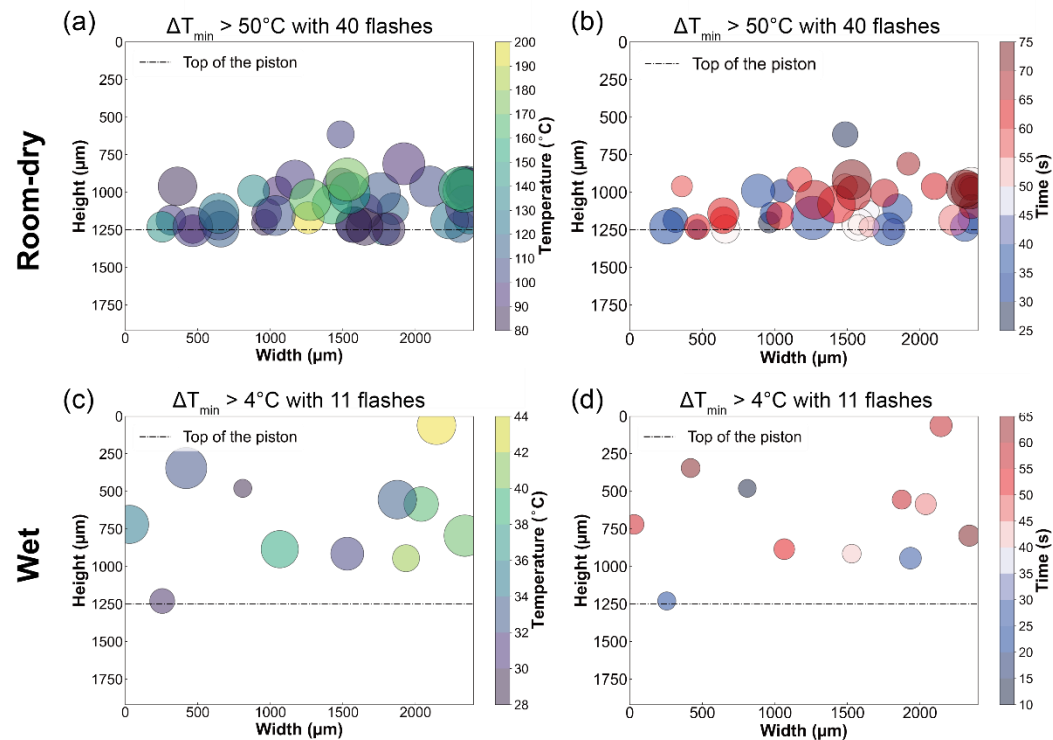
319 **Figure 7.** Spatial and temporal distribution of flashes within the main gouge zone with

320 a minimum temperature rise ΔT (relative to the bulk maximum temperature) larger than

321 50°C and 4°C for the reference experiments of the room-dry (a and b; ID r230 with 40

322 flashes) and wet gouges (c and d; ID r251 with 13 flashes), respectively. Tests

323 performed at 2.5 MPa normal stress and 10 mm/s sliding velocity. Larger dots indicate

324 later occurrence (a, c) or higher temperature rise (b, d).

325

326 **3.4 Estimation of Flash Temperature**

327 Based on the flash-weakening model (e.g. Rice, 2006; Beeler et al., 2008; Proctor

328 et al., 2014; Yao et al., 2018), the flash temperature on an asperity (grain) contact (T_a)

329 within a gouge layer can be expressed as:

$$T_a = T_{bulk} + \frac{\tau_c}{\rho c} \sqrt{\frac{(V/N_a)D_a}{\pi \alpha_{th}}} \tag{1}$$

330 Here, T_{bulk} is the initial bulk temperature of the fault zone, τ_c is the contact shear

331 strength, ρ is the gouge density, and c is the specific heat capacity of the gouge, N_a is

332 the number of asperity contacts sharing the total slip velocity V, D_a is the diameter of

333 the asperity contact, and $\alpha_{th} = K/\rho c$ is the thermal diffusivity of the gouge material,

334 where K is the thermal conductivity. For a first-order estimate, the latent heat of possible

335 reaction (e.g. fluid evaporation) is not considered in the equation. Here we only applied

336 the model to the dry samples. For the dry Ottawa quartz sand with a grain size of 425–

337 500 μm, we took τ_c as ~9–12 GPa (Goldsby and Tullis, 2011), ρ as 2650 kg/m3, c as

338 730 J/kgK and α_{th} as ~1.5 × 10^{-6} m^2/s. Considering the thickness of the shear zone in

339 dry gouges (~4 mm or ~16–20 grains), where ~50% of the gouge layer was involved in

340 shearing (Figure 1d), this results in N_a values ranging from ~8 to 10, which is within a

341 reasonable range, comparable to previous studies (4–10 Yao et al., 2018; 10–20 Rice,

342   2006; 4–13 Proctor et al., 2014; 10 Chen et al., 2023). For D_a, we assumed two different

343   particle packings (hexagonal packing vs. centered cubic packing) to estimate the range

344   of D_a between two spherical grains, assuming Hertzian contact mechanics. Based on

345   the elastic moduli of Ottawa sand (e.g. Erdoğan et al., 2017), for the grain size of 450–

346   500 μm, we adopt average values of D_a as 13, 18, 22, and 25 μm at normal stresses of

347   1, 2.5, 5, 7.5 MPa, respectively. At a normal stress of 2.5 MPa, we take D_a to be 10, 13,

348   17, and 23 μm for grain sizes of 250–300 μm, 300–425 μm, 450–500 μm, and 500–710

349   μm, respectively.

350

351   Figure 8 shows the comparison of the maximum flash temperature obtained from

352   the model prediction and from the measurements for the dry experiments. Overall, the

353   measured values are lower than the predicted ones. Predicted flash temperature

354   increases with increasing slip velocity, normal stress, and grain size, following equation

355   1, but this increasing trend is less (or not) visible in the measurement. The discrepancy

356   between the predicted and measured flash temperature tends to increase with slip

357   velocity and normal stress (Figure 8a, b) but remains relatively consistent with variable

358   grain sizes (Figure 8c).

359

360
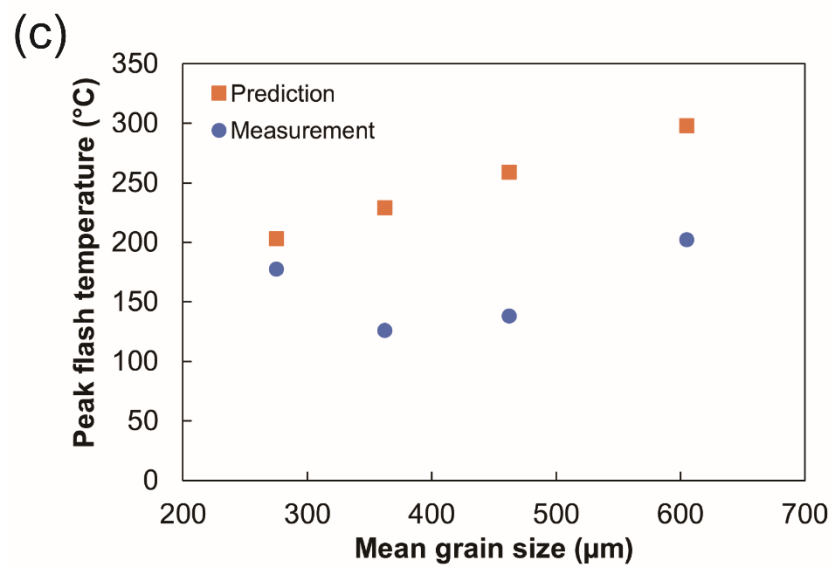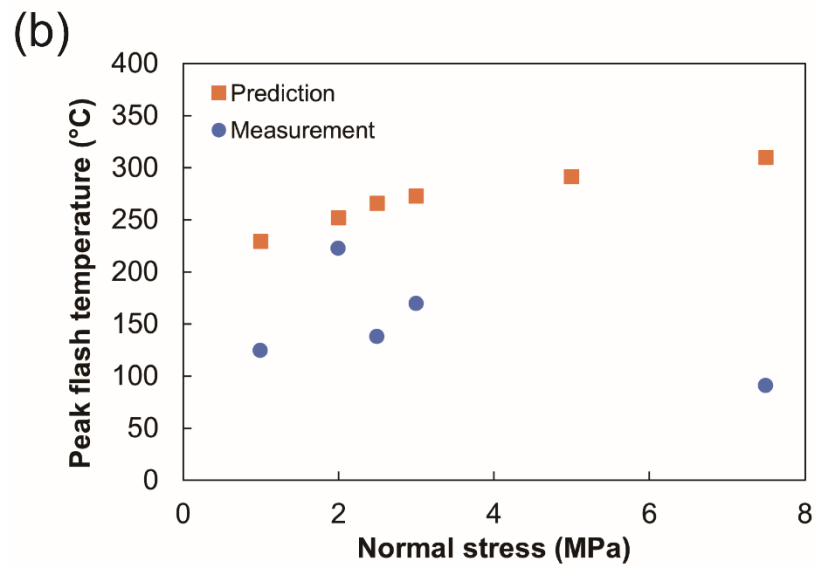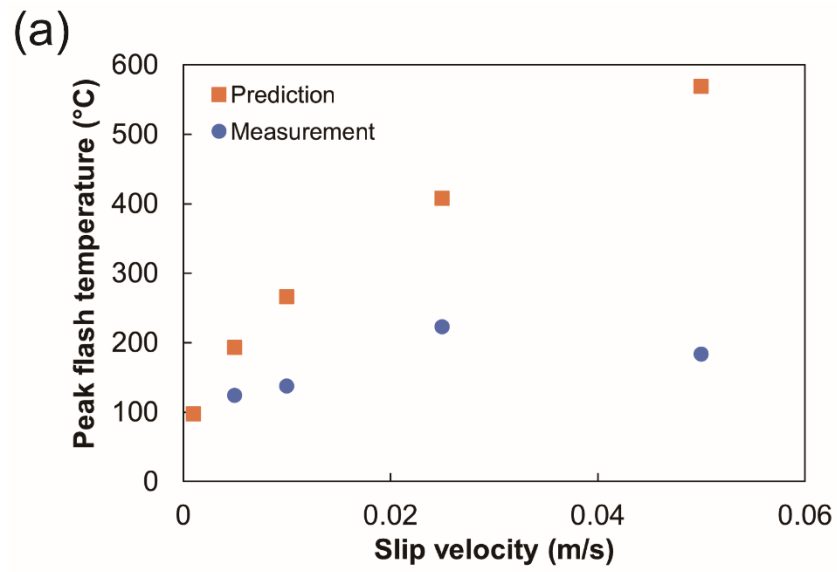
361 **Figure 8.** Comparison of the peak flash temperatures between the prediction based on

362 the flash weakening model (Rice, 2006) and the infrared measurement with different

363 slip velocities (a), normal stresses (b), and grain sizes (c). The measured peak flash

364 temperature at a slip velocity of 1 mm/s is not shown in (a) because the overall measured

365 temperatures are lower than the selected temperature range (60–200°C).

366

367 **4. Discussion**

368 **4.1 Robustness of the Flash Temperature Measurement**

369 In the literature, flash heating is suggested to occur within a short contact lifetime

370 (ms), depending on the scale of asperity contact (typically μm) as well as the sliding

371 velocity at the contact (Rice, 2006). The current setting of the infrared camera can

372 accurately measure thermal information with spatial and temporal resolutions of 15 μm

373 and ~0.83 ms, respectively. This means that the measured temperature might be

374 underestimated if the contact diameter is smaller than 15 μm or if the contact lifetime

375 is shorter than 0.83 ms (e.g. Madding et al., 2007). Another thing to be noted is that

376 even if the grains are perfectly aligned with the window, the contact would still be a

377 distance away from the window, assuming spherical grains. That means that the camera

378 is probably not in focus for the contacts themselves, which would also underestimate

379 the measured temperature. Our measurement of the maximum temperature within the

380 FOV show that multiple peak temperatures (i.e. flashes) with duration of one frame (i.e.

381 0.83 ms) were recorded from the observed region of both the room-dry and wet gouges

382 when the imposed slip velocity is higher than 1 mm/s (Figure 4).

383

384 Figure 9 shows the contact lifetime against the contact diameter D_a, assuming a

385 specific grain size and slip velocity. The D_a is estimated following the method

386   described in section 3.4. The contact lifetime is then obtained from the ratio of D_a to

387   the contact sliding velocity (= imposed slip velocity V / number of asperity contacts

388   N_a). Based on the calculated contact diameter of the asperity D_a (10–25 μm) and the

389   assumed number of asperity contacts N_a (10), the contact lifetime of the asperity for

390   our samples and experimental conditions should range from 10–25 ms to 0.2–0.5 ms at

391   the imposed sliding velocity of 1 mm/s to 50 mm/s, respectively. These ranges lie

392   around the limit of the temporal resolution of the camera, though the contact lifetime

393   for V larger than 5 mm/s appears to be shorter than the duration of one frame, being

394   strongly controlled by the estimated values of the D_a and N_a. This implies that the

395   measured flashes likely resulted from flash heating between grains. Here, we should

396   note that most of the calculated asperity sizes are smaller than the spatial resolution of

397   the camera, suggesting that the actual temperature might be higher than the

398   measurement. Moreover, if the flashes have a shorter duration than the frame duration,

399   their actual temperature was also likely higher than the measured values.

400

401
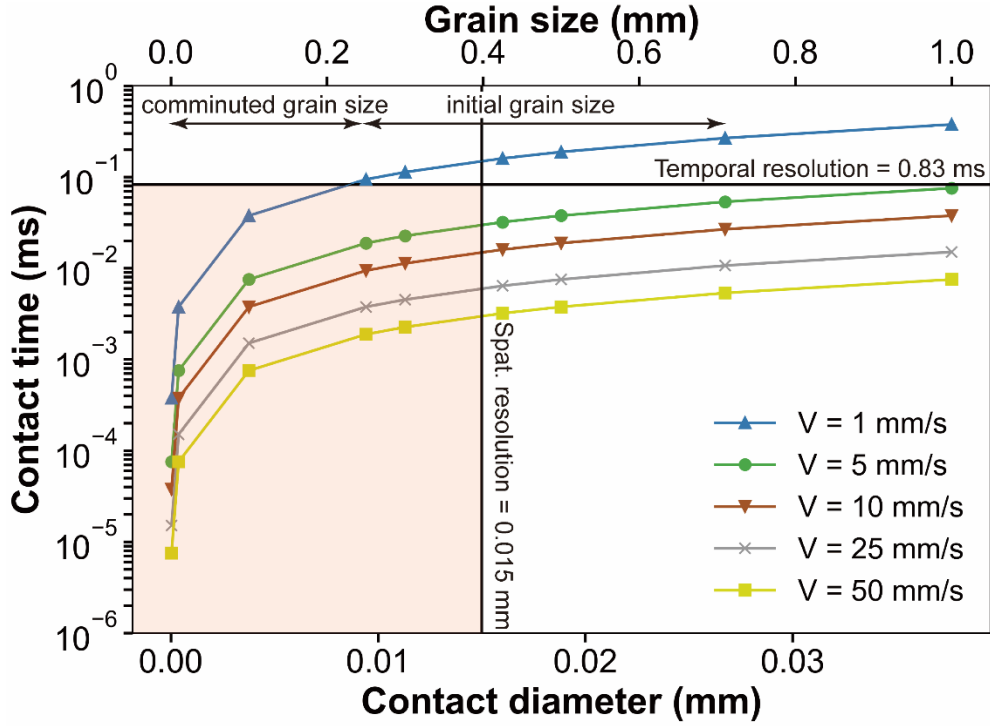
402 **Figure 9.** Contact lifetime against contact diameter D_a for flashes for a specific grain

403 size and slip velocity. The D_a is estimated following the method described in section

404 3.4. N_a is assumed to be 10. The black horizontal line gives a temporal resolution of

405 0.83 ms, and the vertical line has a spatial resolution of 0.015 mm. The light red

406 rectangle region represents the region for which the IR camera with the current settings

407 have neither sufficient spatial nor temporal resolution.

408

409   After filtering out the flashes occurring within the region of the rotating piston, we

410 could still observe a few tens of flashes within the actual gouge zones under both room-

411 dry and wet conditions (Figure 7; Table 1). Among these flashes, we cannot exclude the

412 possibility that some flashes result from the sliding of a grain against the window due

413 to the lateral force and the dragging shear force acting on the grains that are attached to

414 the window. Thus, these flashes might exhibit different characteristics in terms of shape

415 in the thermographs due to the potential of scraping of the grain along the sapphire

416   window. Figure 10 shows three different characteristics of flashes that can be observed

417   from the thermographs. Generally, most of the flashes have a circular shape with the

418   highest temperature at the center which gradually decreases towards the boundary

419   (Figure 10a, b). Some of these flashes are located within the interior of grains (Figure

420   9a), where the individual grain outline can be identified, suggesting the flashes might

421   result from grain-to-window sliding. For other flashes, it is difficult to identify their

422   position relative to the solid grains (Figure 10b). Yet another type of flash displays a

423   tail shape (Figure 10c) which may indicate the existence of grain-to-window flash. With

424   the current data, it is difficult to distinguish whether the flashes were actually generated

425   at grain-to-grain contacts or whether they were mainly related to grain-to-window

426   sliding. To avoid the grain-to-window flashes, improvements in the experimental set-

427   up are required, such as using a curved window to help ensure that the grains can pass

428   along the window without creating temperature flashes. Another possibility might be to

429   include an IR-transparent low-friction coating on the window.

430

431
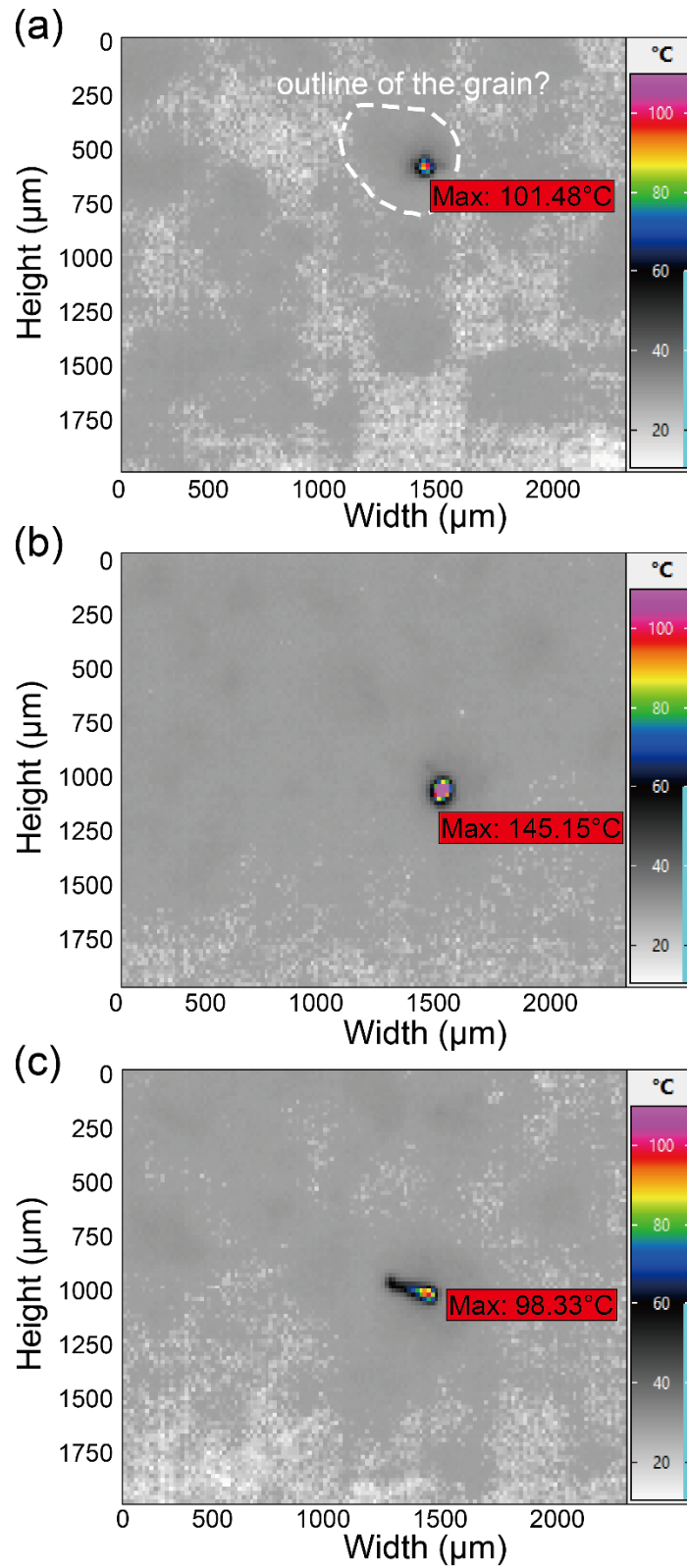
Figure 10. Thermographs with a flash identified in the actual gouge zone, as obtained

from the reference room-dry experiment (r230) at displacements of 293 mm (a), 676

mm (b), and 526 mm (c).

435

436   Comparing our measurements with model predictions shows that measured flash

437   temperatures are consistently lower than predicted, and that the discrepancy increases

438   with normal stress and slip velocity (Figure 8). As discussed above, the limited spatial

439   and temporal resolution of the IR camera may contribute to these differences by

440   underestimating the true peak temperatures. Another possible explanation is that the IR

441   camera only captures temperatures at the flanks of the gouge layer or grain contacts,

442   rather than at their centers. Because stress concentrations at contact asperities generate

443   extremely steep temperature gradients, even a small offset from the central portion of

444   the contact results in significantly lower measured temperatures. This geometric

445   constraint likely contributes to the observed discrepancy between measured and

446   predicted flash temperatures. We argue that the increasing discrepancies could be

447   related to the process of grain size reduction during frictional sliding, and/or possibly

448   the setting of the IR temperature ranges. As can be seen in the measured particle size

449   distribution of the deformed sample (Figure 1g), abundant fine grains were generated

450   during the experiment. The initial grain size (425–500 μm) is reduced to a minimum

451   value of ~50 nm, with the largest proportion of grains smaller than the starting material

452   having a size of 10 μm. In addition, the proportions of fine grains are systematically

453   larger at a higher normal stress and slip velocity. This indicates that high normal stress

454   and slip velocity increase the degree of grain size reduction, which leads to a decrease

455   in asperity size D_a and a possible increase in N_a (at a constant thickness of the localized

456   zone) as well as an increased contribution of fracture energy from grain comminution.

457   The decrease in asperity size would affect affect our ability to resolve flash temperatures

458   in space and time, because smaller contacts persist for shorter durations (Figure 9). The

459 increase in fracture energy suggests a potential energy sink that is not converted into

460 heat, although we found that this contribution is negligible compared to the frictional

461 work. If grain size reduction is one of the reasons causing the increasing variations, this

462 implies that the measured flash temperatures should decrease with displacement due to

463 the limitation of the spatial resolution or the peak temperatures might move away from

464 the zone of grain size reduction. However, we do not observe these behaviors. To

465 characterize the flash temperature distribution in the gouge layer robustly, multiple

466 temperature ranges or a combined temperature range should be utilized in multiple

467 repeat experiments (Barbery et al., 2021). Despite all this, our results still show some

468 dependence of flash temperature on slip velocity and grain size.

469

470 **4.2 Mechanical Behaviors under Room-Dry and Wet Conditions**

471 We observed that the measured average temperature and flash temperatures can

472 reach up to ~73°C and ~220°C, respectively, under room-dry conditions (Table 1).

473 Despite high flash temperatures, suggesting the high effectiveness of flash heating, the

474 room-dry gouges do not show any significant weakening which remains at a constant

475 friction level of 0.6 (typical quasi-steady friction for quartz; Byerlee, 1978). This might

476 be explained by the relatively low measured and predicted flash temperatures as

477 compared to the softening (i.e. melting) temperature of quartz (~1720°C, Spray, 1992).

478

479 By contrast, the water-saturated gouges reveal slip weakening accompanied by

480 fluid pressure increase at relatively high normal stresses (>2.5 MPa) and slip velocities

481 (>10 mm/s), while the average and flash temperature rises are only up to ~9°C and

482 ~80°C, respectively (Figure 4, 5, and 6; Table 1). Firstly, this suggests that temperature

483 increase can be strongly limited by the presence of water, though the effect of water on

484 the IR signal has not been considered in the data processing. Secondly, the above

485 temperature increases of 9°C and 80°C are insufficient to account for the observed fluid

486 pressure increase (3.5–7 MPa). We expect the bulk fluid pressure increase to be less

487 than 1 MPa, taking a reasonable range for the thermal pressurization factor Λ (e.g.

488 0.075–0.11 MPa/°C for quartz-rich gouges; Hunfeld et al., 2021). On this basis, we

489 suggest that the mechanism causing slip weakening in the wet samples is most likely

490 associated with compaction-induced pressurization (compaction softening - Oohashi et

491 al., 2011), which is supported by the data shown in Figure 3.

492

493   At the same time, however, other candidate mechanisms related to the presence of

494 water, such as thermomechanical pore fluid pressurization (Rice, 2006; Badt et al.,

495 2020), flash pressurization resulting from local thermal pressurization at grain contacts

496 induced by flash heating (e.g. Chen et al., 2023; Yao et al., 2018; Hung et al., 2025),

497 and/or the water/vapor phase transition (e.g. Chen et al., 2017) cannot be completely

498 excluded. Silica-gel lubrication due to amorphization of silica and gel formation via

499 shearing and comminution in the presence of moisture (Di Toro et al., 2004; Goldsby

500 and Tullis, 2002) might be another possible candidate for the dynamic weakening seen

501 in fast shearing of wet quartz materials. To test these hypotheses, we need to ensure the

502 gouge sample is well-compacted before the initiation of a high slip velocity to prevent

503 significant compaction during the experiment. This is typically achieved by applying a

504 conditioning stage (i.e. shear at low slip velocity) to the gouge layer. However, this was

505 intentionally not included in the current study because the initial grain size reduction

506 and associated comminution products would limit thermal radiation from grain contacts.

507 In addition, thermal flashes would become difficult to measure due to the shorter

508 asperity contact lifetime.

509

510 **5. Conclusions and Future Work**

511 In this study, we perform rotary-shear friction experiment on sheared fault gouge

512 analogues with a high-speed infrared camera to characterize flash temperatures induced

513 by flash heating at grain contact scales and their dependence on normal stress, slip

514 velocity, and grain size. The important findings in the present work are as follows:

515 1. We can successfully monitor and quantify flash heating with instantaneous

516 temperature rises occurring in an experimental fault gouge under room-dry and

517 wet conditions.

518 2. The presence of pore water likely limits flash temperature rise, though the extent

519 of the effect is unclear due to uncertainties in the extent of IR absorption of thermal

520 signatures by the water phase.

521 3. Flash heating can be effective in dry gouge at a medium velocity (5 cm/s) but is

522 insufficient to cause dynamic slip weakening in a dry gouge-filled fault because

523 the flash temperature is too low to reach the softening temperature of the gouge

524 grains.

525 4. The slip weakening effects that we observed in our wet experiments but not in dry

526 tests are best explained by compaction softening, though a contribution from

527 thermal pressurization at some scale cannot be eliminated.

528 5. We have experimentally demonstrated that the flash temperature depends on slip

529 velocity and grain size, to some extent, in broad agreement with theoretical

530 predictions.

531

532   Final, we listed future work to further improve our understanding of flash heating

533   in a sheared granular layer on the basis of the current results:

534   1.   Using normal high-speed camera to observe the sliding velocity at grain-to-grain

535   contacts.

536   2.   Investigating the dependence of peak flash temperature on other particle

537   parameters like grain shape (round vs. angular), grain roughness, as well as

538   different background fluid pressures and pore fluids.

539

540   **Data availability**

541   All raw data can be provided by the corresponding authors upon request.

542

543   **Author contribution**

544   Conceptualization: André R. Niemeijer; Data curation: Chien-Cheng Hung, André R.

545   Niemeijer; Formal analysis: Chien-Cheng Hung, André R. Niemeijer; Funding

546   acquisition: André R. Niemeijer; Investigation: Chien-Cheng Hung, André R.

547   Niemeijer; Methodology: Chien-Cheng Hung, André R. Niemeijer; Project

548   administration: Chien-Cheng Hung, André R. Niemeijer; Resources: André R.

549   Niemeijer; Supervision: André R. Niemeijer; Validation: Chien-Cheng Hung;

550   Visualization: Chien-Cheng Hung; Writing (original draft preparation): Chien-Cheng

551   Hung; Writing (review and editing): André R. Niemeijer

552

553   **Competing interests**:

554   The authors declare that they have no conflict of interest.

555

556   **Financial support**

This work is part of the research programme DeepNL, financed by the Dutch Research Council (NWO); Grant: DEEP.NL.2018.040. Additional support for the purchase of the high-speed infrared camera was provided by the Nederlandse Aardolie Maatschappij (NAM).

References

Acosta, M., Passelègue, F. X., Schubnel, A., & Violay, M. (2018). Dynamic weakening during earthquakes controlled by fluid thermodynamics. Nature communications, 9(1), 3074.

Badt, N. Z., Tullis, T. E., Hirth, G., & Goldsby, D. L. (2020). Thermal pressurization weakening in laboratory experiments. Journal of Geophysical Research: Solid Earth, 125(5), e2019JB018872.

Barbery, M. R., Chester, F. M., & Chester, J. S. (2021). Characterizing the distribution of temperature and normal stress on flash heated granite surfaces at seismic slip rates. Journal of Geophysical Research: Solid Earth, 126(5), e2020JB021353.

Barbery, M. R., Chester, F. M., & Chester, J. S. (2023). Investigating dynamic weakening in laboratory faults using multi-scale flash heating coupled with mm-scale contact evolution. Journal of Geophysical Research: Solid Earth, 128(12), e2023JB027110.

Beeler, N. M., Tullis, T. E., & Goldsby, D. L. (2008). Constitutive relationships and physical basis of fault strength due to flash heating. Journal of Geophysical Research: Solid Earth, 113(B1).

Brantut, N., & Platt, J. D. (2017). Dynamic weakening and the depth dependence of earthquake faulting. Fault zone dynamic processes: Evolution of fault properties during seismic rupture, 171-194.

582   Chen, J., Hunfeld, L. B., Niemeijer, A. R., & Spiers, C. J. (2023). Fault weakening

583   during short seismic slip pulse experiments: The role of pressurized water and

584   implications for induced earthquakes in the Groningen gas field. Journal of Geophysical

585   Research: Solid Earth, 128(2), e2022JB025729.

586   Di Toro, G., Goldsby, D. L., & Tullis, T. E. (2004). Friction falls towards zero in

587   quartz rock as slip velocity approaches seismic rates. Nature, 427(6973), 436-439.

588   Di Toro, G., Niemeijer, A., Tripoli, A., Nielsen, S., Di Felice, F., Scarlato, P., ...

589   & Mariano, S. (2010). From field geology to earthquake simulation: a new state-of-the-

590   art tool to investigate rock friction during the seismic cycle (SHIVA). Rendiconti Lincei,

591   21, 95-114.

592   Erdoğan, S. T., Forster, A. M., Stutzman, P. E., & Garboczi, E. J. (2017). Particle-

593   based characterization of Ottawa sand: Shape, size, mineralogy, and elastic moduli.

594   Cement and concrete composites, 83, 36-44.

595   Goldsby, D. L., & Tullis, T. E. (2002). Low frictional strength of quartz rocks at

596   subseismic slip rates. Geophysical research letters, 29(17), 25-1.

597   Goldsby, D. L., & Tullis, T. E. (2011). Flash heating leads to low frictional

598   strength of crustal rocks at earthquake slip rates. Science, 334(6053), 216-218.

599   Hangx, S. J., & Brantut, N. (2019). Micromechanics of high-pressure compaction

600   in granular quartz aggregates. Journal of Geophysical Research: Solid Earth, 124(7),

601   6560-6580.

602   Hunfeld, L. B., Chen, J., Niemeijer, A. R., Ma, S., & Spiers, C. J. (2021). Seismic

603   slip-pulse experiments simulate induced earthquake rupture in the Groningen gas field.

604   Geophysical research letters, 48(11), e2021GL092417.

605   Hung, C. C., Niemeijer, A., Aretusini, S., Spagnuolo, E., Chen, J., & Hamers, M.

606   (2025). Dynamic weakening in sandstone-derived fault gouges during simulated small-

607 magnitude earthquakes under variable loading and environmental conditions.

608 Geophysical Journal International, 241(2), 1009-1028.

609 Kohli, A. H., Goldsby, D. L., Hirth, G., & Tullis, T. (2011). Flash weakening of

610 serpentinite at near-seismic slip rates. Journal of Geophysical Research: Solid Earth,

611 116(B3).

612 Korkolis, E. (2019). Rotary shear experiments on glass bead aggregates: Stick-

613 slip statistics and parallels with natural seismicity (Doctoral dissertation, UU Dept. of

614 Earth Sciences).

615 Madding, R. P., Orlove, G. L., & Lyon, B. R. (2007, April). The importance of

616 spatial resolution in IR thermography temperature measurement: three brief case

617 studies. In Proceedings of SPIE, the International Society for Optical Engineering (pp.

618 654108-1). Society of Photo-Optical Instrumentation Engineers.

619 Niemeijer, A., Di Toro, G., Griffith, W. A., Bistacchi, A., Smith, S. A., & Nielsen,

620 S. (2012). Inferring earthquake physics and chemistry using an integrated field and

621 laboratory approach. Journal of Structural Geology, 39, 2-36.

622 Oohashi, K., Hirose, T., & Shimamoto, T. (2011). Shear-induced graphitization

623 of carbonaceous materials during seismic fault motion: Experiments and possible

624 implications for fault mechanics. Journal of Structural Geology, 33(6), 1122-1134.

625 Proctor, B. P., Mitchell, T. M., Hirth, G., Goldsby, D., Zorzi, F., Platt, J. D., & Di

626 Toro, G. (2014). Dynamic weakening of serpentinite gouges and bare surfaces at

627 seismic slip rates. Journal of Geophysical Research: Solid Earth, 119(11), 8107-8131.

628 Rice, J. R. (2006). Heating and weakening of faults during earthquake slip.

629 Journal of Geophysical Research: Solid Earth, 111(B5).

630 Saber, O. (2017). Development and Characterization of a high-speed material-

631 testing machine, and experimental Analysis of frictional flash Heating and dynamic

632   Weakening in rock (Doctoral dissertation).

633   Spagnuolo, E., Plümper, O., Violay, M., Cavallo, A., & Di Toro, G. (2015). Fast-

634   moving dislocations trigger flash weakening in carbonate-bearing faults during

635   earthquakes. Scientific Reports, 5(1), 16112.

636   Tullis, T. E. (2015). Mechanisms for friction of rock at earthquake slip rates.

637   Yao, L., Ma, S., Niemeijer, A. R., Shimamoto, T., & Platt, J. D. (2016a). Is

638   frictional heating needed to cause dramatic weakening of nanoparticle gouge during

639   seismic slip? Insights from friction experiments with variable thermal evolutions.

640   Geophysical Research Letters, 43(13), 6852-6860.

641   Yao, L., Ma, S., Platt, J. D., Niemeijer, A. R., & Shimamoto, T. (2016b). The

642   crucial role of temperature in high-velocity weakening of faults: Experiments on gouge

643   using host blocks with different thermal conductivities. Geology, 44(1), 63-66.

644   Yao, L., Ma, S., Chen, J., Shimamoto, T., & He, H. (2018). Flash heating and

645   local fluid pressurization lead to rapid weakening in water-saturated fault gouges.

646   Journal of Geophysical Research: Solid Earth, 123(10), 9084-9100.